

UC San Diego

UC San Diego Previously Published Works

Title

Adhesion tunes speed and persistence by coordinating protrusions and extracellular matrix remodeling.

Permalink

<https://escholarship.org/uc/item/1rq09886>

Journal

Developmental Cell, 58(15)

Authors

Leineweber, William
Fraley, Stephanie

Publication Date

2023-08-07

DOI

10.1016/j.devcel.2023.05.013

Copyright Information

This work is made available under the terms of a Creative Commons Attribution License, available at <https://creativecommons.org/licenses/by/4.0/>

Peer reviewed



HHS Public Access

Author manuscript

Dev Cell. Author manuscript; available in PMC 2024 August 07.

Published in final edited form as:

Dev Cell. 2023 August 07; 58(15): 1414–1428.e4. doi:10.1016/j.devcel.2023.05.013.

Adhesion tunes speed and persistence by coordinating protrusions and extracellular matrix remodeling

William D. Leineweber¹, Stephanie I. Fraley, Ph.D.^{*,1}

¹Department of Bioengineering; University of California, San Diego, La Jolla, CA, 92093; United States

Summary

Cell migration through 3D environments is essential to development, disease, and regeneration processes. Conceptual models of migration have been developed primarily on the basis of 2D cell behaviors, but a general understanding of 3D cell migration is still lacking due to the added complexity of the extracellular matrix. Here, using a multiplexed biophysical imaging approach for single-cell analysis of human cell lines, we show how the subprocesses of adhesion, contractility, actin cytoskeletal dynamics, and matrix remodeling integrate to produce heterogeneous migration behaviors. This single-cell analysis identifies three modes of cell speed and persistence coupling driven by distinct modes of coordination between matrix remodeling and protrusive activity. The framework that emerges establishes a predictive model linking cell trajectories to distinct subprocess coordination states.

Graphical Abstract

*Lead contact, correspondence to sifraley@ucsd.edu.

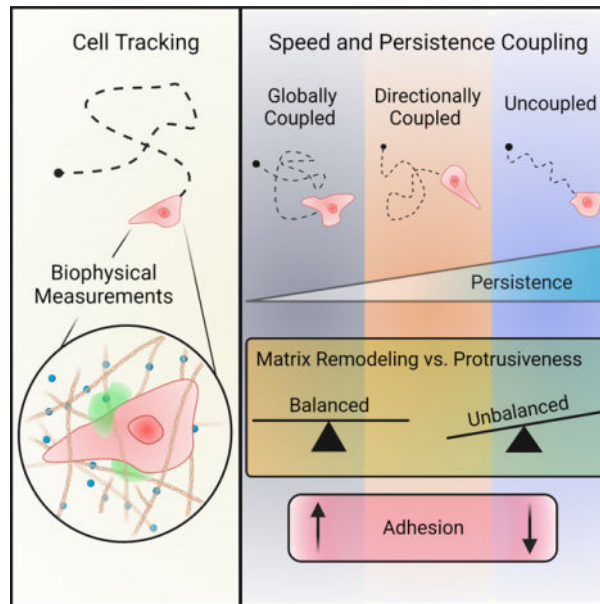
Author contributions

W.D.L. and S.I.F. designed the experiments. W.D.L. performed all the experiments and data analysis. Data interpretation was conducted by W.D.L. and S.I.F. Both authors contributed to the writing and editing of the manuscript.

Publisher's Disclaimer: This is a PDF file of an unedited manuscript that has been accepted for publication. As a service to our customers we are providing this early version of the manuscript. The manuscript will undergo copyediting, typesetting, and review of the resulting proof before it is published in its final form. Please note that during the production process errors may be discovered which could affect the content, and all legal disclaimers that apply to the journal pertain.

Declaration of interests

The authors declare no competing interests.



Blurb:

Leineweber and Fraley develop an approach to measure multiple types of interactions between individual cells and their surrounding 3D matrix while also tracking migration. By modeling this multiscale data, they accurately predict migration heterogeneity and identify a link between cell-matrix adhesion and the uncoupling of cell speed and persistence.

Introduction

Cell migration is a complex behavior that emerges from biophysical and biochemical interactions between thousands of molecular parts within and between cells and their environment. Comprehensively measuring migration machinery across space and time is not currently possible, so pairing experiments with modeling efforts is crucial to advancing our understanding of cell migration. Most studies have been limited to 2D cell migration on flat surfaces, where cells flatten and become easy to image due to the absence of a 3D extracellular matrix (ECM). In these studies, the complexities of the migration machinery have been abstracted into three predominant subprocesses that run concurrently and are spatially coordinated: protrusion, adhesion, and contraction.¹ Many features of cell morphodynamics and migration on 2D substrates can be explained by treating these subprocesses as functional modules connected in a simplistic circuit²⁻⁴ originally predicted by Abercrombie, which goes as follows: (1) protrusion of the leading edge, (2) formation of strong adhesions at the leading edge, (3) aging adhesions at the trailing edge that are (4) released by contraction of the cell leading to forward movement.⁵ More recent modeling efforts have focused on gaining a molecular level understanding of each subprocess.⁶ Still, this conceptual framework does not account for the major role that the ECM plays in confining and resisting cell movement.

Navigation through 3D tissue-like environments is physiologically relevant for many migratory cells; however, the technical challenges inherent to studying 3D migration are formidable. Particular challenges include microscopy and image analysis limitations in 3D and the increased complexity brought about by additional modes of migration in 3D versus 2D.^{7–10} Predictions of cell behavior in 3D based on data acquired in 2D are often unreliable because signaling and mechanical parameters do not always directly translate from 2D to 3D.^{11–17} Moreover, an additional subprocess is necessary to consider for migration through 3D environments: extracellular matrix (ECM) remodeling.^{18–21} *In vivo* interstitial pore sizes range from ~0.025–0.1 μm in diameter,²² and those of the basement membrane range from ~0.6–3.85 μm .²³ These pore sizes are smaller than most cell bodies (10–100 μm in diameter) and cell nuclei (3–7 μm in diameter when deformed during MMP-independent migration)²¹. So, cells migrating through tissues must remodel the matrix by either physical or biochemical mechanisms. Many 3D cell migration studies have used low density matrices that have much larger pore sizes than the ECM *in vivo*^{21,24–28}, which enables cells to migrate without remodeling. Indeed, it has been demonstrated that MMP-independent migration is a function of pore size.²¹ In confining ECM, where pore sizes are representative of *in vivo* tissues, it is not well understood how the processes of matrix remodeling, protrusion, adhesion, and contraction are integrated to produce different modes of 3D migration. Additionally, the relationships between these processes are unclear in the context of 3D cell migration.

Without an integrated framework for whole cell 3D migration in confining ECM built on the four key subcellular processes, it remains difficult to distinguish the origins of migration heterogeneity. For example, cells of the same type can display significantly different migration behaviors, even in ostensibly the same 3D environment.^{18,28–31} Does cell migration heterogeneity arise from fundamentally different interrelations between the subprocesses, or can it be explained by a threshold or shift in activity of one or several of the subprocesses? Experts argue that answering this question may be the most important contribution toward unraveling the mechanisms of migration.³²

An integrated framework would also help to contextualize seemingly contradictory results from experimental perturbations.¹ The pathways controlling migration are often nonlinear and redundant. They may also feedback on each other, making it exceedingly difficult to address questions through single-plex molecular experiments or mechanochemical models. For example, several different combinations of physical mechanisms can be fitted to explain the same experimental behaviors, but directly testing them can be impossible. Obtaining sufficient physical and biochemical constants required for accurate models in 3D systems can be difficult to impossible. An alternative approach for modeling how cells process subcellular information into whole cell behaviors is to use a data-driven methodology based on the quantitative effects of perturbations to key high-level process modules.^{33–38}

Here we present a data-driven model of 3D cell migration in confining ECM built on integrated measurements of protrusion, adhesion & contraction (traction), and matrix remodeling in single migrating cells. Single cell tracking data revealed three modes of coupling between cell speed and persistence, which were linked to distinct combinations of cell-ECM interactions. This work represents an advancement in our understanding of how

heterogeneous migration can arise and provides actionable insights into engineering cell migration behavior.

Results

Cell migration is heterogeneous and less common behaviors can be enriched by perturbing biophysical processes that dictate cell-ECM interactions

To determine whether different levels of migration subprocess activity or different interrelations between the subprocesses account for heterogeneous migration behaviors within a given cell population (Fig. 1A), it is necessary to study “average” cells as well as “rare” cells that display less common behaviors. The distributions of migration behavior for cells migrating in confining 3D collagen type I matrices can be characterized by the persistent random walk (PRW) model^{13,39}, which uses the mean squared displacement (MSD) of cells to attribute values of cell speed (S) and persistence time (P) to migrating cells (eqn 1). The other parameters in this equation include the time lag (τ), dimensionality of the tracking (n), and the positioning error (SE).

$$MSD(\tau) = nS^2P^2(e^{-\tau/P} + \tau/P - 1) + SE \quad (\text{eqn 1})$$

For example, MDA-MB-231 (MDA) display a wide range of total displacements (10.32–183.72 μm), speeds (0.022–0.395 $\mu\text{m}/\text{min}$), and persistence times (0.431–994.846 min). Across multiple cell types, including MDAs, HT-1080s, and HFF-1s, both total cell displacement and cell speed are logarithmically distributed (Fig. 1B–C), and persistence shows a bimodal logarithmic distribution (Fig. 1D). This suggests a general distribution of cell migration behavior in confining 3D collagen matrices and shows that capturing less common migration behaviors requires extensive sampling.

We hypothesized that inhibitors targeting the individual processes of contractility (ROCKi), matrix remodeling (MMPi), cytoskeletal protrusion (F-ACTINi), and adhesion (ITGB1i) could enrich for different regimes of migration behaviors within the general distribution. As anticipated, these treatments shifted the peak of the distributions of displacement, speed, and persistence compared to the vehicle control while remaining within the general ranges (Fig 1E–H). For example, ROCKi, MMPi, and F-ACTINi increased the population of low-persistence cells and shifted the cell speed distribution towards lower values. ITGB1i inhibition, on the other hand, increased the number of highly persistent cells and shifted the cell speed distribution towards faster cells. To confirm that the effects of the small molecule inhibitors have similar effects of more targeted knockdowns, we also assayed cells with ROCK1 knocked down (Fig. S1 A–E) and ITGB1 knocked down (Fig. S1 F–I). The effects of the more specific knockdowns were more subtle, but trended in similar directions as the inhibitor treatments. Cumulatively, these results suggest that changes in the level of activity of one or more processes could potentially account for naturally occurring migration heterogeneity. However, it is not clear whether shifts in activity are also accompanied by different interrelations between the core subprocesses.

Cell-ECM interaction measurements capture whole-cell biophysical behavior

To determine the interrelations between the core subprocesses and migration outcomes, each process must be simultaneously measured in individual cells as they migrate through the ECM. Since the activity of a given process is not well described by any single measurement, we integrated nine imaging-based measurements of cell-ECM interactions to read out various aspects of subprocess activity. These measurements were captured by timelapse z-stack imaging in three fluorescent channels for MDAs in 3D collagen as follows: blue fluorescent matrix-embedded beads enabled measurement of percent (%) bead movers, maximum bead displacement, and instantaneous bead displacement as readouts of cellular contractility against the matrix; green fluorescence from dye-quenched collagen (DQ) measured the remodeling of the matrix by cells; red fluorescent protein expression in cells allowed us to measure instantaneous cell displacement, protrusion rate, lifetime, and max length as readouts of cytoskeletal activity; and the ratio of the average instantaneous bead displacement over the average instantaneous cell displacement gave a measure of the coupling between a cell and the surrounding ECM (Table 1). We will subsequently refer to this imaging platform and resulting measurements as “biophysical imaging”.

3D volume view time-series demonstrate the technique’s ability to capture heterogeneous subprocess activity between individual cells, where the differences in cell protrusive activity (red), bead movement (blue), and matrix remodeling (green) are easily visualized (Fig. 2A–B). The cell in Fig 2A remains rounded, with minimal protrusive, contractile, or matrix remodeling activity. In contrast, the cell in Fig 2B retracts a protrusion, resulting in displacement of the microbeads, and has a strong DQ signal indicating matrix remodeling. In some instances, we found cells remodeling the matrix by protruding into it and retracting (Video S1). In other cases, matrix degradation was localized at the cell body near the neck of longer protrusions (Video S2). These results demonstrate the utility of this imaging approach to measure heterogeneous cell-ECM interactions at the single cell level.

Next, we measured how cell-ECM interactions changed in response to inhibition of each of the core subprocesses using the biophysical imaging platform. Since each inhibitor treatment shifted the distribution of cell migration behavior (Fig. 1F–H), we hypothesized that they would also shift cell-ECM interaction distributions such that distinct cell states could be identified. Inhibitors were used as opposed to molecular knockdowns to obtain more robust effects on the individual biophysical processes, while still resulting in migration behavior in the range of vehicle cells (Fig. 1F–H). 3D reconstructions representing an average cell from each inhibitor treatment are shown (Fig. 2C) and distributions of cell-ECM interaction responses are plotted (Fig. 2D–L). Compared to vehicle-treated cells, F-ACTINi cells (green) displaced the matrix less (Fig. 2D,F), moved slower (Fig. 2G), remodeled the matrix less (Fig. 2H), and extended few protrusions (Fig. 2I–K). ROCKi (blue) decreased the extent of matrix displacement (Fig. 2D,F), cell movement (Fig. 2G), and matrix remodeling (Fig. 2H), but increased cytoskeletal protrusion activity (Fig. 2I–K). MMPi cells (red) were slower on average than vehicle cells (Fig. 2G), but surprisingly did not remodel the matrix to a significantly lesser extent (Fig. 2H). MMPi treatment targeted the main family of ECM collagenases, so the insignificant decrease in the DQ measurement compared to control cells was unexpected. As an additional check, we confirmed that the DQ signal is an accurate

readout of matrix degradation by using a degraded-collagen hybridizing peptide (CHP) as a secondary measurement (Fig. S2). Finally, ITGB1i cells increased their instantaneous cell speed compared to the vehicle control. In total, each inhibitor treatment differentially regulated cell-ECM interactions and shifted cell migration distributions in distinct ways.

Principal component analysis (PCA) on this cell-ECM interaction dataset clustered cells in the same treatment conditions relatively well, despite the heterogeneity observed (Fig. 2M, Table 2). The separation of the data along PC1 was driven by fairly equal contributions from instantaneous cell displacement, protrusion rate, instantaneous bead displacement, and the displacement ratio (Fig. 2N). Interestingly, PC1 also seemed to order treatment groups from least to most migratory (compare Fig. 2E to Fig. 1F,G). PC2 separation was driven by protrusion length and lifetime in the positive direction, and instantaneous bead displacement and displacement ratio in the negative direction. This axis helped to separate the ROCKi group from the F-ACTINi and MMPi populations. To test the generalizability of this approach, we also performed biophysical imaging on HT1080 cells and mapped these measurements onto the principal components (Fig. S3 A). HT1080 cells clustered together and were most similar to the ITGB1i treatment group (Fig. S3 B–K), and we confirmed via western blot that HT1080s have less ITGB1 protein than MDAs. These results highlight this imaging platform's capacity to detect molecular differences between cells. Together, these results show that the nine cell-ECM measurements obtained from biophysical imaging can discriminate between cell states associated with distinct migration distributions arising from intra- and intercellular heterogeneity as well as molecular inhibition of migration processes.

Cell trajectories are well-modeled by the persistent random walk model when speed and persistence are coupled

Coupling between cell speed and persistence is not universal in 3D migrating cells

—With our biophysical imaging method established, we next sought to understand how cell-ECM interactions map to long term cell migration trajectories. We devised a two-stage experimental approach where cells were tracked for 8 hours followed by biophysical imaging for 1 hour. Direct comparisons could then be made between long-term migration behavior and snapshots of the cell-ECM interaction state within the same cell. In this integrated experimental protocol, cell trajectories (Fig. 3A) followed similar trends as those from our earlier cell tracking experiments (Fig. 1E), where fluorescent beads and DQ were not included in the matrix. ITGB1-inhibited cells were again the most migratory, while F-actin inhibited cells were mostly non-migratory. MMP and ROCK inhibition decreased migration compared to the vehicle condition.

Since two migration parameters, speed and persistence, are sufficient to describe and predict cell migration trajectories, we fit the MSD of individual cell trajectories to the PRW model (Fig. 3B) to extract values for cell speed (S) and persistence time (P) (eqn1). We found that many of the analyzed cells, though not all, followed a migration regime wherein speed and persistence were coupled (Fig. 3C). This coupling fits a general form of the “universal coupling between speed and persistence” (UCSP) equation that has been previously reported (eqn 2).⁴⁰ Fitting the UCSP equation to cells displaying this coupling behavior produced a robust fit ($R^2 = 0.862$, Fig. 3C, circled data).

$$P = A * e^{\lambda * S} + C \quad (\text{eqn 2})$$

A subpopulation of cells, mostly from the ITGB1-inhibited population, did not follow this coupling law, and in fact appear to display a negative relationship between speed and persistence (Fig 3C, data outside of circle). Interestingly, we do not see uncoupling of S and P at low P. These results show that cell speed and persistence time are often, though not universally, coupled in migrating cells in confining 3D matrices. Since inhibition of ITGB1 produced the most cells in the decoupled migratory regime, this suggests that adhesion plays an important role in determining persistence time and in coupling persistence to speed.

Cell-ECM measurements predict cell speed and persistence in coupling regime.—

Since PCA, a linear data transformation method, clustered cell states (Fig. 2E) and ordered them along PC1 similar to the order of their migration distributions (Fig. 1F–H), we reasoned that a simple linear regression could model the relationship between cell-ECM interactions and migration. We also considered that cells following the UCSP law may rely on a fundamentally different configuration of cell-ECM interactions than the cells that don't obey this relationship. Therefore, we used partial least squares regression (PLSR) to ask which cell-ECM interactions are the best predictors of S and P for cells that follow the UCSP behavior. All 511 possible combinations of the nine cell-ECM interaction measurements were tested as the independent variable matrix to fit the dependent variable S or P, and leave-one-out cross validation was performed to account for over-fitting. The resulting goodness of fit (R^2) and predictive ability (Q^2) of every possible regression model was calculated, and the model with the highest Q^2 was chosen as the optimal model. Applying this approach with P as the dependent variable yielded an optimal model with an $R^2 = 0.524$ and a $Q^2 = 0.449$ (Fig. 3D). The optimal model for P accounts for about 52.5% of the variance using only two PLS components (Fig. 3E), and consists of bead-cell displacement ratio, protrusion length, instantaneous bead displacement, maximum bead displacement, DQ, and percent bead mover measurements (Fig. 3F). The observed vs. fitted values of z-normalized P values shows that the model performs well across the different inhibitor treatments (Fig. 3G).

PLSR analysis was also performed for S (Fig 3H–K), which revealed that S is best predicted by a model consisting of the same cell-ECM measurements used for P, but without needing bead displacement or percent bead movers ($R^2 = 0.529$, $Q^2 = 0.469$). The loading for bead-cell displacement ratio correlates with low speed and persistence, while high maximum bead displacement, percent bead movers, and DQ are most correlated with enhanced speed and persistence (Fig. 3F,J). The finding that these interaction measurements are the most predictive of speed and persistence update the UCSP model that previously reported only actin flow was required to predict migration behavior.⁴⁰ Using only the three protrusion measurements representing actin cytoskeletal activity in the regression model (Fig. S4) achieved less predictive power for P ($R^2 = 0.305$, $Q^2 = 0.201$) and S ($R^2 = 0.292$, $Q^2 = 0.180$), and was suboptimal compared to the more comprehensive regressions (Fig. 3G, K). In the updated model, the inclusion of bead-cell displacement ratio, DQ, and multiple bead measurements indicate that the processes of adhesion, matrix remodeling, and

contractility are key determining factors along with actin-based protrusion dynamics for 3D cell migration.

To test the performance of these models, we simulated PRW migration trajectories using *S* and *P* values predicted from cell-ECM interactions (Fig. 3L). We then compared these to simulated PRW trajectories using the *S* and *P* values extracted from cell MSDs (Fig. 3M) and to the original real trajectories of the cells (Fig. 3A). Trajectories predicted from cell-ECM interactions recapitulate the global effects of the inhibitor treatments and also the heterogeneity within each population. This generalizability of the model was next tested by incorporating HT1080s, which predominantly followed the *S* and *P* coupling regime (Fig. S5 A–B). The optimal model to predict HT1080 speed and persistence used similar biophysical measurements as that of the MDAs (Fig. S5 C–D). Importantly the model generated by MDAs and agnostic to HT1080s predicted HT1080 speed and persistence nearly identically as the model generated using both MDAs and HT1080s (Fig. S5 E–F). The cell-ECM measurements required for the optimal model demonstrate the necessity of capturing the coordination between cytoskeletal protrusions, contractility, matrix remodeling, and adhesion for this mode of cell migration.

Trajectories of cells whose speed and persistence are not well coupled are modeled by a distinct set of cell-ECM interactions.

The PLSR model that predicts cell migration in the UCSP regime (Fig. 3D–L) does not achieve a good fit for cells outside of this regime, suggesting that these globally uncoupled cells occupy a distinct cell-ECM interaction state. These cells had longer persistence times than those in the coupled range, but their cell speeds were within the range of the other measured cells (Fig. 4A). Since these cells are highly persistent, we reasoned that they may be better modeled using the anisotropic persistent random walk (APRW) model. APRW takes into account cells with preferred migration directions by deconvolving the migration into a primary direction and an orthogonal non-primary direction, each with a persistence and speed (*P*₁,*S*₁ and *P*₂,*S*₂, respectively)³⁹. When the cells with globally uncoupled speed and persistence were fit using the APRW model, a subset of these cells displayed coupling in the primary direction of migration (Fig. 4B). Coupling was also observed for some cells along the non-primary direction axis (Fig. 4C). Therefore, cells that do not display global coupling between speed and persistence, as modeled by PRW, can still display coupling behavior along primary or non-primary directions of migration, which is captured by the APRW model.

Cell-ECM interaction state in anisotropic *S* vs. *P* coupling—We next asked whether a distinct set of cell-ECM interactions were associated with globally uncoupled (APRW) cell migration. We further delineated cells that couple speed and persistence along the primary direction of APRW migration (red squares) from those that do not (blue triangles). PLSR of cells with speed and persistence coupling along the primary migration axis (*P*₁ and *S*₁) were well-modeled by only a few combinations of cell-ECM interactions (Fig. S6A). The optimal model for persistence in the primary direction consisted of instantaneous cell displacement, *DQ*, protrusion length, and percent bead movers (Table S1, Fig. S6A–D). *DQ*, protrusion length, and percent bead movers, were also contributors

to persistence in the PRW model, though in the APRW model the coefficient for protrusion length becomes negative, indicating that anisotropic persistent cells tend to have shorter protrusions (Table S1). Additionally, P1 relied on only one bead measurement, indicating a decreased reliance on matrix displacement in determining persistence. P2 was predicted by maximum bead displacement, protrusion rate, DQ, and protrusion lifetime.

Speed in the primary direction (S1) of APRW coupled cells is best predicted by cell-ECM interactions (Fig. S6G) that are quite distinct from those that predict speed in PRW coupled cells (Fig. 3J), sharing only DQ as a component. S1 instead needed maximum bead displacement, protrusion rate, protrusion lifetime, and percent movers for optimal predictive performance. S2 model components overlap strongly with S1, only substituting instantaneous bead displacement and protrusion rate for maximum bead displacement and protrusion lifetime (Fig. S6O). APRW trajectories predicted from cell-ECM interactions were very similar to those simulated from MSD fits of the real trajectory data (Fig. 4D).

Cell-ECM interaction state of cells with predominantly uncoupled S vs. P—

Cells that did not display global coupling between S and P in the PRW model or in the primary direction in the APRW model could be regressed using a distinct set of cell-ECM interactions. Only four combinations of measurements had R^2 vs. Q^2 values to predict primary persistence. This consisted of DQ, protrusion lifetime, protrusion length, instantaneous cell displacement, and bead-cell displacement ratio (Fig. S7A–D). Cells in this regime tend to have highly linear trajectories, which were predicted well by our model (Fig. 4E). High protrusion rate paired with low bead speed, instantaneous cell displacement, DQ, and protrusion lifetime predicted high P1 (Fig. S7C). The PLSR model for S1 (Fig. S7E–H) was similar to that for the APRW coupled model (Fig. S7E–H). This indicates that in both subpopulations of the globally uncoupled cells, cell speed determination is independent from the factors that dictate cell persistence. Thus, the status of S and P coupling defines three different cell migration modes that rely on distinct combinations of cell-ECM interactions to achieve their persistence and speed (Fig. 4F,G). Only matrix remodeling (DQ) was required to predict speed and persistence for all three populations, demonstrating the importance of this measurement when analyzing 3D migration modes.

Matrix remodeling coordination with adhesion and cell protrusion define distinct modes of cell migration

To visualize key changes between different migration modes, cell-ECM interactions were plotted for cells undergoing PRW Coupled, APRW Coupled, or APRW Uncoupled migration. We found no significant differences in any individual measurement between these groups, though the two APRW groups displayed slight differences compared to the PRW group due to their enrichment with predominantly ITGB-1-inhibited cells (Fig. 5A–I). Analysis of the correlations among cell-ECM measurements in each group of cells revealed key changes in how subprocesses are coordinated (Fig. 5 J–L). Strikingly, PRW coupled cells have strong positive correlations between multiple bead and protrusion measurements, as well as DQ and instantaneous cell displacement (Fig. 5J). These contrast with the more heterogeneous correlations in the two APRW groups (Fig. 5K,L). Notably, the strong positive correlations between protrusion rate and DQ becomes weaker in the APRW

Coupled cells, and eventually negatively correlated in the APRW Uncoupled cells (Fig. 5M). Thus, the randomness of the walk is associated with the balance between cell protrusive activity and matrix degradation.

Through this correlation analysis, distinct differences in subprocess coordination also emerged between the two APRW groups. There was a significant switch in the relationship between DQ and protrusion length (Fig. 5N). APRW coupled cells showed a positive correlation between these measurements, but APRW uncoupled cells showed a negative correlation. Representative micrographs of cells from these two groups exemplify these relationships (Fig. 5O). Cells that couple speed and persistence in the primary direction of migration (APRW coupled) show more matrix remodeling with more protrusive activity. Cells with uncoupled speed and persistence, on the other hand, tend to be more rounded if they are remodeling the matrix and more elongated if they are not. These patterns are enriched for ITGB1-inhibited cells. These findings prove that cells rely on different combinations of cell-ECM interactions to migrate, defined by three random walk modes of migration. Therefore, it is possible to use cell tracking data to infer cell-ECM interaction and, by extension, the overall biophysical state of the cell.

Discussion

Cell migration trajectories to predict associated cell-ECM interaction state using S&P coupling as a classifier

In this study, we used a data-driven approach to discover how cell-ECM interactions produce heterogeneous migration behaviors. This was achieved through an integration of cell-ECM interaction reporters and cell tracking, which revealed relationships between motility subprocesses and whole cell behavior. While previous studies applied different walk models to describe heterogeneous migration behavior in 3D environments⁴¹, ours connects the walk behavior to underlying cellular subprocesses coordination. We show that confined 3D migration can be classified into three modes of speed and persistence coupling, and we developed a predictive model for each mode that links cell-ECM interaction state to cell trajectories. For all migration modes, matrix remodeling was essential, and yet no one subprocess measurement could achieve high predictive capability in isolation. This modeling approach could serve as an important tool towards integrating disparate conceptual models of cell migration that comprise the Central Dogma. For example, the adhesion-based model holds that cell speed is well-predicted by a biphasic relationship with adhesion, and that this relationship can be explained by adhesion-promoted forces pushing the front and resisting motion at the rear of the cell according to a ‘molecular clutch’ model of focal adhesion-actin-myosin dynamics.^{6,42–51} The actin-based model holds that speed is predicted by actin flow and its effect on polarity signals.⁴⁰ None of the well-accepted conceptual models indicate a role for matrix remodeling, likely because they originate primarily from experiments on 2D substrates or permissive 3D environments, and they do not address how migration subprocesses integrate to produce heterogeneous behaviors. Indeed, prior works seeking to understand the coupling between speed and turning (persistence) of immune cells moving in 3D *in vivo*^{52,53} have not considered the role of ECM remodeling. Nonetheless, there is ample evidence that matrix remodeling is required for their *in vivo* migratory

functions. For example, T-cells require MMPs to penetrate into infected tissue and contribute to significant tissue remodeling.⁵⁴

An important outcome of our models is the ability to reliably predict cell trajectories of multiple cell types from measurements of cell-ECM interactions. The reverse is also true, in that our models enable the prediction of cell-ECM interaction state from cell trajectories. This lends insight into how the subprocesses of migration can produce different regimes of cell speed and persistence coupling that generate migration trajectories with different extents of anisotropy. Establishing this link is important towards building multi-scale models of cell migration and generating hypotheses for further mechanistic studies.

The degree of migration anisotropy is enhanced with S&P uncoupling.

This work presents a conceptual model that integrates two migration frameworks: 1) speed and persistence coupling and 2) persistent random walk models. The integration of these models revealed that speed and persistence are not universally coupled, and that the extent of coupling is directly related to the randomness of migration. Cells that follow the original UCSP law could only be accurately predicted within the PRW framework. The remaining cells were found to be either globally uncoupled or uncoupled only in the non-primary axis of migration, which can be modeled by the APRW framework. These classifications were necessary to link migration behavior with cell-ECM interaction measurements and achieve high predictive power. Integrating these two paradigms of cell migration modeling represents an important step towards building comprehensive models of cell migration that capture heterogeneity.

Loss of adhesion uncouples S&P.

We observed that many cells display coupling between speed and persistence, which has previously been described as the UCSP law and has been reproduced in multiple experimental^{55,56} and theoretical models.^{57,58} However, a population of cells, mostly within the ITGB1-inhibited condition, did not follow the UCSP and instead displayed a negative relationship between speed and persistence. These cells are more persistent at lower-than-expected cell speeds, implicating adhesion as a key mediator of speed and persistence coupling. Increased persistence may be consistent with the model of integrin function in which inhibition of $\beta 1$ integrin activity feeds back on MT1-MMP surface levels and localization. Previous population-level studies have shown that on average, inhibition of $\beta 1$ integrin activity tends to induce its association with MT1-MMP and reduce recycling, leading to accumulation of both integrin and MT1-MMP on the cell surface.⁵⁹ However, in our single-cell experiments, distinct subpopulations within the ITGB1-inhibited condition may represent cells with different levels of ITGB1-inhibition response or different initial levels of ITGB1 and MT1-MMP. The extent to which the level and activity of ITGB1 and MT1-MMP are balanced on the surface of the cell could explain the distinct coordination modes of protrusions and matrix remodeling we observed (Fig. 5 M–O).

Blocking adhesion enhanced cell speed on average, indicating that the cells were originally slower migrating because they were in a higher adhesion state (Fig. 1E–H, Fig. S8). This reinforces the established biphasic relationship between adhesion and speed and echoes

observations that cells having less ECM adhesion are more migratory.^{60,61} In 2D, the force the cell exerts via actomyosin contraction at sites of focal adhesion determines adhesion plaque growth, maturation, and stability.^{62,63} In 3D, it has been proposed that contractility must be locally balanced with ECM stiffness to stabilize adhesions.⁶⁴ When we diminished the ability of integrins to bind to the ECM, we would expect the stability of adhesions to be compromised, resulting in faster turnover and a less stable force balance between the contractile machinery and the ECM. It is interesting that in this condition where we might expect multiple highly localized force balance instabilities, we see higher persistence of migration. Perhaps with less competition from other adhesion sites, the fewer stable adhesions drive the polarization of the cell.

The degree of S&P uncoupling is associated with the imbalance of protrusion rate and matrix remodeling.

Coupling between speed and persistence can be global, or broken into anisotropic primary and non-primary directions of migration. Applying the PRW model distinguishes globally coupled cells versus those that are not. Within the PRW coupled cell population, we found a strong positive correlation between protrusion rate and instantaneous cell displacement, which is consistent with the UCSP model that actin flow stabilizes cell speed. However, protrusion rate was also significantly positively correlated with DQ signal. This could suggest that protrusions physically enhanced degradation, which is supported by the fact that inhibiting actin polymerization or contractility lowered DQ signal (Fig. 2H) but MMPi treatment did not significantly impact DQ signal or protrusions (Fig 2I–K). This finding is consistent with other reports, such as how Latrunculin B decreases the ability of MDA-MB-231 cells to bundle collagen I around the cell, more so than marimastat⁶⁵ and that the mechanical plasticity of the matrix can facilitate protease-independent migration.⁶⁶ However, differences in trafficking of MMPs to the membrane cannot be ruled out.

In contrast to the globally coupled cells, the uncoupled population had a negative correlation between protrusion rate and DQ. This suggests that speed and persistent coupling depends upon balanced activity between protrusion rate and matrix remodeling. High levels of one without the other leads to uncoupled migration, which leads to anisotropic migration.

When globally uncoupled cells are further divided within the APRW framework into S&P coupled or uncoupled in the primary direction, we found that the uncoupled cells drove the negative relationship between protrusion rate and matrix remodeling, while the APRW coupled cells had no significant correlation between these cell-ECM interactions. Therefore, there appears to be a progressive transformation of the relationship from strongly positive, to no correlation, to strongly negative as cells are globally coupled, anisotropically coupled, or uncoupled. This implicates matrix remodeling as playing a central role in determining S&P coupling. This, paired with the necessity of the DQ measurement for each of the regression models (Fig. 4F–G), strengthens the argument that matrix remodeling is a key determinant of cell migration in confining 3D conditions.

Matrix remodeling is a necessary input to every predictive model we discovered, and its coordination with protrusive activity of cells helps differentiate between S&P coupling behaviors. The overarching conceptual model we propose captures these essential motility

subprocess coordination modes and could be useful as a basis to model processes in which cell migration trajectory is important, such as cancer invasion or immune cell homing. Future studies to elucidate the molecular mechanisms underlying each coordination mode will enable the next generation of physical models of migration.

Mapping Speed and Persistence Coupling to Modes of Migration

The 2.5mg/ml collagen I matrices used in this study have an average pore size of $2\mu\text{m}^2$, though the 99th percentile of sizes reaches $22\mu\text{m}^2$. When pore cross sectional area is less than 10% of a cell's nucleus, then migration becomes dependent on matrix remodeling.²¹ Unperturbed cells within these matrices primarily behaved in a mesenchymal fashion that is characterized by spindle-like protrusions, cell-ECM adhesion, actomyosin contractility, and proteolytic ECM remodeling. Conversely, ameboid migration is typically classified by a more rounded cell body, low adhesion, low matrix remodeling activity, high contractility, and high migration.^{67,68} Inhibiting adhesion or matrix remodeling can shift cells into a more ameboid state.^{69–71} Our findings shed light on these migration mode definitions. We found that blocking ITGB1 enriched for cells with uncoupled speed and persistence and enhanced motility, suggesting that uncoupling is characteristic of amoeboid migration. The most uncoupled cells, APRW Uncoupled, displayed a negative correlation between matrix remodeling and protrusion. In this mode, migrating cells protrude and squeeze through permissible pores in the ECM, while cells encountering smaller pores remain more rounded and remodel the matrix to move. On the other hand, broadly inhibiting MMPs did not significantly affect matrix remodeling and did not enrich for uncoupled cells. Rather, the majority remained in the PRW Coupled mode where matrix remodeling positively correlated with protrusion rate and bead movement, suggesting that PRW Coupled cells may rely heavily on physical matrix remodeling supported by adhesion to the ECM. We also found that the APRW Coupled mode falls between PRW Coupled and APRW Uncoupled in terms of protrusion and matrix remodeling coordination and may represent transition regime between mesenchymal and ameboid.

Limitations of the Study

Cell migration is a context-dependent behavior, and therefore the conclusions drawn from this study may not apply to all 3D cell migration modes. Future studies exploring other cell types and different matrix compositions will contribute to our understanding of generalizable principles of motility subprocess coordination states that drive diverse migration behaviors. Additionally, distinguishing between physical and enzymatic ECM remodeling mechanisms will be important to achieving this goal.

STAR Methods

Resource Availability

Lead Contact—Further information and requests for resources and reagents should be directed to and will be fulfilled by the lead contact, Stephanie Fraley (sifraley@ucsd.edu).

Materials availability—This study did not generate new unique reagents.

Data and code availability

- Original western blot images have been deposited at Mendeley and are publicly available as of the date of publication. The DOI is listed in the key resources table. Microscopy data reported in this paper will be shared by the lead contact upon request.
- All original code has been deposited at Mendeley and is publicly available as of the date of publication. DOIs are listed in the key resources table.
- Any additional information required to reanalyze the data reported in this paper is available from the lead contact upon request.

Experimental model and subject details

Cell Lines—MDA-MB-231, HT1080, and HFF-1 cells (ATCC, Manassas, VA) were cultured in high glucose Dulbecco's modified Eagle's medium supplemented with 10% (v/v), fetal bovine serum (FBS, Corning, Corning, NY) and 0.1% gentamicin (ThermoFisher Scientific, Waltham, MA) and maintained at 37°C and 5% CO₂ in a humidified environment during culture and imaging. The cells were passaged every 2–3 days as required. Lentiviral transduction was performed using pLV-mCherry, which was a gift from Pantelis Tsoulfas (Addgene plasmid # 36084).

Method Details

3D collagen gel formation—3D collagen I matrices were prepared in a manner similar to that described previously.^{18,28} Cells suspended in culture medium were mixed 1:1 (v/v) with 10X reconstitution buffer. Next, blue fluorescent carboxylated microspheres (1 μm, ThermoFisher Scientific, Waltham, MA) were added to the cell-gel solution at 1:50 (v/v) of the final gel volume. DQ collagen (ThermoFisher Scientific, Waltham, MA)⁷² was added to achieve a final concentration of 100 μg/mL, followed by soluble rat tail type I collagen in acetic acid (Corning, Corning, NY) to reach the desired final collagen concentration of 2.5 mg ml⁻¹. 1 M NaOH was used to normalize pH and promote polymerization in a volume proportional to the collagen concentration (pH 7.0). Thoroughly mixed gels were then pipetted into custom made PDMS wells mounted on glass bottom dishes (Fluorodish, World precision Instruments). Gels were polymerized at 37°C in a humidified incubator for at least 30 minutes before media was added to cover the gel.

Biophysical imaging—Cells were imaged immediately after cell tracking using an TI inverted microscope equipped with a 40X (NA: 1.15) long working distance objective (Nikon Instruments Inc., Melville, NY) equipped with a controlled temperature, CO₂, and humidity chamber. Each cell was imaged for 1 hour at 4-minute intervals. For each timepoint, a z-stack through the cell body was taken at 1.5 μm steps in four channels - blue, green, red, and reflection - to image the fluorescent beads, DQ collagen, cells, and ECM architecture, respectively. The resulting image files were saved as.tif stacks and opened in ImageJ for processing (NIH, Bethesda, Maryland, USA, <https://imagej.nih.gov/ij/>). Only cells whose primary axis of spreading was in the XY plane were used for quantification. As we have shown previously, this simplifies the cell and bead tracking to 2D geometry without a significant loss of information^{18,73}. Maximum intensity projections (MIPs) of the z-stacks

were generated at each time-point to create a 2D time series for each channel of each cell for analysis. 3D reconstructions of the z-stacks for solely visualization purposes were completed using IMARIS software (Oxford Instruments, Abindon, UK).

Biophysical inhibitors—Inhibitor experiments were performed using ROCK inhibitor Y-27632 (10 μ M from 10mM stock in DMSO), Latrunculin B (5 μ M from 5mM stock in DMSO), and the combined Marimastat (10 μ M from 10mM stock in DMSO) and GM6001 (10 μ M). Inhibitors were added to the cell solution used during gel preparation and in the media added to the top of the collagen gels after gelation. ITGB-1-blocking antibody P5D2⁷⁴ was optimized for concentration (5 μ g/ml, Fig. S8) and added solely to the cell solution and not the media (Figure S8). The vehicle and ITGB-1-blocking media contained 0.1% (v/v) DMSO.

Quantification of protrusion dynamics—Cell protrusion tracking is a well-established approach for quantifying the cytoskeletal dynamics of a cell^{13,75,76}. Protrusions were manually tracked in ImageJ using the MIP time series of the cell. The time duration of each protrusion was tracked frame-by-frame from initial protrusion extension to complete retraction. The mean protrusion length and time duration of the protrusions was calculated for each cell. The number of cell protrusions greater than 1 μ m observed during the 1 hr imaging period was used for the “protrusions rate” measurement. For cells that did not form any protrusions during the imaging, the mean max length of protrusions and protrusion lifetime were both zero.

Quantification of matrix remodeling—DQ collagen increases in fluorescent intensity when cleaved by collagenase activity^{77,78}. To quantify the degree of degradation, the fluorescence intensity of a 10 μ m band surrounding the cell was measured for each frame using ImageJ. The total intensity values were summed and divided by the total area of the bands to get a mean fluorescence intensity surrounding the cell body using a custom MATLAB script. This value was then divided by the mean fluorescence intensity of the background to get the Signal/Background ratio.

Quantification of traction force microscopy—Traction force microscopy is a technique that uses fiducial markers in the ECM to quantify how a cell is interacting with the surrounding microenvironment^{79–81}. Bead tracking was done in the blue channel MIP using the Mosaic plugin in ImageJ. The Results table, which contains the XY coordinates for each bead in the field of view for each time point, was saved and analyzed in a custom MATLAB script to identify the beads that moved during the time-lapse (Figure 2C). First, a filter was applied to analyze only trajectories of beads that were tracked through all time points. Second, the displacement at each time point from the initial point was calculated for each bead. Next, to identify beads that were actively pulled by the cells we used a moving standard deviation approach where we calculated the standard deviation of consecutive points across the entire bead trajectory. With this, we were able to identify the parts of the trajectory that significantly deviate from the rest, which corresponds to a deformation in the matrix. The “% bead movers” measurement reflects the percent of the total beads in the image frame that met this criteria. The max bead displacement between frames and

the instantaneous bead speed over the time course were averaged together for all the beads meeting the movement threshold to generate the “mean max bead displacement” and “mean instantaneous bead speed” values for each cell.

Bead-cell speed ratio measurement—The bead-cell speed ratio is a measurement that describes cell-ECM movement coupling⁷³. It is calculated as the ratio between the instantaneous bead speed and the instantaneous cell speed. It can be understood as the opposite of a slip ratio, which is a measure typically applied to automobiles to describe the slipping behavior of a wheel against a road surface. Instantaneous cell speed was calculated by tracking single cells using Metamorph software (Molecular devices, San Jose, CA). Cell tracking produces XY coordinates for the cell body at every time-lapse frame and instantaneous speed is computed as the distance traveled by the cell between consecutive frames (Figure 2C). For bead trajectories, we performed the same analysis as for cell trajectories to obtain a frame-by-frame speed. Bead-cell speed ratio was calculated as the mean instantaneous bead speed divided by the mean instantaneous cell speed of the filtered beads used in the displacement tracking.

Principal component analysis and regression—Principal component analysis of the cell-ECM interaction dataset used the z-normalized nine cell-ECM measurements for the cells analyzed across the vehicle and inhibitor treatments. PCA was performed using GraphPad Prism’s PCA tool.

Long-term live cell tracking—Long-term cell tracking was conducted using MDA-MB-231 WT cells in the 2.5mg ml⁻¹ collagen I matrices without beads or DQ. Imaging was conducted on a Nikon Ti-Eclipse Epifluorescent Microscope at 10x equipped with a Tokai Hit stage-top incubation system. Brightfield images were taken every 15 minutes over the time course. Cells that moved within the imaging plane were tracked using Metamorph software to generate 2D trajectories of migration, as is standard in the field^{39,82}. 2D tracking was performed for cells that remained in the z-plane of tracking²⁸ to optimize spatial accuracy, imaging throughput, and analysis throughput. The mean squared displacement was calculated from the trajectories using a custom MATLAB script.

Fitting MSD to persistent random walk model—The migration parameters of persistence (P), speed (S), and positioning error (SE) were determined using a nonlinear least squares regression of the persistent random walk model (eqn 1) adapted from previous work by Wu, Pei-Hsun, et al.³⁹

Hybrid biophysical and cell tracking experimental setup—Gels were prepared in the same fashion as described in the “3D collagen gel formation” section. The samples were imaged on the epifluorescent microscope used in the long-term live cell tracking experiments. The acquisition settings were modified to reduce phototoxicity by setting the time interval to 4 minutes and the z-step size to 1.5 μm . Cells were tracked in brightfield from hours 5–13 post-embedding at 15-minute intervals, followed by 1 hr of biophysical imaging.

Partial Least Squares Regression—Biophysical measurements from cells in the regression dataset were analyzed as described above, as was the cell tracking and fitting to random walk models. A custom MATLAB script was used to perform the PLSR analysis of these cells using the built-in function `plsregress()`. First, the dataset was curated to remove cells that divided, died, or migrated out of frame during the tracking or biophysical imaging. Next, every combination of the nine biophysical measurements were used as the input matrix to find the R2 and Q2 scores when fitting to P, S, and SE. The regression with the optimal Q2 was chosen as the model to analyze the component loadings, percent variance explained, and the observed. vs. fitted values. Simulated trajectories were calculated using MATLAB scripts modified from Wu, Pei-Hsun, et al.³⁹. PC scores of the original biophysical dataset were used as the inputs for the regression equations to generate values of P, S, and SE for each cell imaged. For cells modeled with APRW the same analysis was performed for the primary and non-primary P, S, and SE.

Quantification and statistical analysis

Principal component analysis (PCA) and all statistics were performed using Graphpad Prism. Student-t-tests were used to compare the means two populations. One-way ANOVA analyses followed by the appropriate post-tests were performed to compare three or more populations. See figure captions for details of statistical analyses and post-tests.

Supplementary Material

Refer to Web version on PubMed Central for supplementary material.

Acknowledgements

Support for this study was provided by National Science Foundation CAREER award MCB-1651855 to S.I.F., National Science Foundation grant DMS-1953469, and American Cancer Society Research Scholar Grant RSG-21-033-01-CSM to S.I.F.. We would like to thank the UC San Diego School of Medicine Microscopy Core, which is supported by the National Institute of Neurological Disorders and Stroke grant P30NS047101.

References

1. Ridley AJ, Schwartz MA, Burridge K, Firtel RA, Ginsberg MH, Borisy G, Parsons JT, and Horwitz AR (2003). Cell migration: integrating signals from front to back. *Science* 302, 1704–1709. [PubMed: 14657486]
2. DiMilla PA, Barbee K, and Lauffenburger DA (1991). Mathematical model for the effects of adhesion and mechanics on cell migration speed. *Biophys. J* 60, 15–37. [PubMed: 1883934]
3. Herant M, and Dembo M (2010). Form and function in cell motility: from fibroblasts to keratocytes. *Biophys. J* 98, 1408–1417. [PubMed: 20409459]
4. Tranquillo RT, Lauffenburger DA, and Zigmond SH (1988). A stochastic model for leukocyte random motility and chemotaxis based on receptor binding fluctuations. *J. Cell Biol* 106, 303–309. [PubMed: 3339093]
5. Abercrombie M (1980). The Croonian Lecture, 1978 - The crawling movement of metazoan cells. *Proc. R. Soc. Lond. B Biol. Sci* 207, 129–147.
6. Chan CE, and Odde DJ (2008). Traction dynamics of filopodia on compliant substrates. *Science* 322, 1687–1691. [PubMed: 19074349]
7. Charwat V, Schütze K, Holthöner W, Lavrentieva A, Gangnus R, Hofbauer P, Hoffmann C, Angres B, and Kasper C (2015). Potential and limitations of microscopy and Raman spectroscopy for live-cell analysis of 3D cell cultures. *J. Biotechnol* 205, 70–81. [PubMed: 25687101]

8. Chiu C-L, Aguilar JS, Tsai CY, Wu G, Gratton E, and Digman MA (2014). Nanoimaging of focal adhesion dynamics in 3D. *PLoS One* 9, e99896. [PubMed: 24959851]
9. Driscoll MK, and Danuser G (2015). Quantifying modes of 3D cell migration. *Trends Cell Biol.* 25, 749–759. [PubMed: 26603943]
10. Schneckenburger H, and Richter V (2021). Challenges in 3D live cell imaging. *Photonics* 8, 275.
11. Baskaran JP, Weldy A, Guarin J, Munoz G, Shpilker PH, Kotlik M, Subbiah N, Wishart A, Peng Y, Miller MA, et al. (2020). Cell shape, and not 2D migration, predicts extracellular matrix-driven 3D cell invasion in breast cancer. *APL Bioeng* 4, 026105. [PubMed: 32455252]
12. Cukierman E, Pankov R, Stevens DR, and Yamada KM (2001). Taking cell-matrix adhesions to the third dimension. *Science* 294, 1708–1712. [PubMed: 11721053]
13. Fraley SI, Feng Y, Krishnamurthy R, Kim D-H, Celedon A, Longmore GD, and Wirtz D (2010). A distinctive role for focal adhesion proteins in three-dimensional cell motility. *Nat. Cell Biol* 12, 598–604. [PubMed: 20473295]
14. Fraley SI, Feng Y, Giri A, Longmore GD, and Wirtz D (2012). Dimensional and temporal controls of three-dimensional cell migration by zyxin and binding partners. *Nat. Commun* 3, 719. [PubMed: 22395610]
15. Friedl P, Entschladen F, Conrad C, Niggemann B, and Zänker KS (1998). CD4+ T lymphocytes migrating in three-dimensional collagen lattices lack focal adhesions and utilize beta1 integrin-independent strategies for polarization, interaction with collagen fibers and locomotion. *Eur. J. Immunol* 28, 2331–2343. [PubMed: 9710211]
16. Janmey PA, Hinz B, and McCulloch CA (2021). Physics and Physiology of Cell Spreading in Two and Three Dimensions. *Physiology* 36, 382–391. [PubMed: 34704856]
17. Scott KE, Fraley SI, and Rangamani P (2021). A spatial model of YAP/TAZ signaling reveals how stiffness, dimensionality, and shape contribute to emergent outcomes. *Proc. Natl. Acad. Sci. U. S. A* 118. 10.1073/pnas.2021571118.
18. Ranamukhaarachchi SK, Modi RN, Han A, Velez DO, Kumar A, Engler AJ, and Fraley SI (2019). Macromolecular crowding tunes 3D collagen architecture and cell morphogenesis. *Biomaterials science* 7, 618–633. [PubMed: 30515503]
19. Scott KE, Rychel K, Ranamukhaarachchi S, Rangamani P, and Fraley SI (2019). Emerging themes and unifying concepts underlying cell behavior regulation by the pericellular space. *Acta Biomater.* 96, 81–98. [PubMed: 31176842]
20. Trappmann B, Baker BM, Polacheck WJ, Choi CK, Burdick JA, and Chen CS (2017). Matrix degradability controls multicellularity of 3D cell migration. *Nat. Commun* 8, 371. [PubMed: 28851858]
21. Wolf K, Te Lindert M, Krause M, Alexander S, Te Riet J, Willis AL, Hoffman RM, Figdor CG, Weiss SJ, and Friedl P (2013). Physical limits of cell migration: control by ECM space and nuclear deformation and tuning by proteolysis and traction force. *J. Cell Biol* 201, 1069–1084. [PubMed: 23798731]
22. Zhou A, Qu J, Liu M, and Tso P (2020). The Role of Interstitial Matrix and the Lymphatic System in Gastrointestinal Lipid and Lipoprotein Metabolism. *Front. Physiol* 11, 4. [PubMed: 32038309]
23. Howat WJ, Holmes JA, Holgate ST, and Lackie PM (2001). Basement membrane pores in human bronchial epithelium: a conduit for infiltrating cells? *Am. J. Pathol* 158, 673–680. [PubMed: 11159204]
24. Lämmermann T, Bader BL, Monkley SJ, Worbs T, Wedlich-Söldner R, Hirsch K, Keller M, Förster R, Critchley DR, Fässler R, et al. (2008). Rapid leukocyte migration by integrin-independent flowing and squeezing. *Nature* 453, 51–55. [PubMed: 18451854]
25. Petrie RJ, Koo H, and Yamada KM (2014). Generation of compartmentalized pressure by a nuclear piston governs cell motility in a 3D matrix. *Science* 345, 1062–1065. [PubMed: 25170155]
26. Cavanagh H, Kempe D, Mazalo JK, Biro M, and Endres RG (2022). T cell morphodynamics reveal periodic shape oscillations in three-dimensional migration. *Journal of The Royal Society Interface* 19. 10.1098/rsif.2022.0081.
27. Fraley SI, Wu P-H, He L, Feng Y, Krisnamurthy R, Longmore GD, and Wirtz D (2015). Three-dimensional matrix fiber alignment modulates cell migration and MT1-MMP utility by spatially and temporally directing protrusions. *Sci. Rep* 5, 14580. [PubMed: 26423227]

28. Velez DO, Tsui B, Goshia T, Chute CL, Han A, Carter H, and Fraley SI (2017). 3D collagen architecture induces a conserved migratory and transcriptional response linked to vasculogenic mimicry. *Nat. Commun* 8, 1651. [PubMed: 29162797]
29. Chen K, Ozturk K, Contreras RL, Simon J, McCann S, Chen WJ, Carter H, and Fraley SI (2021). Phenotypically supervised single-cell sequencing parses within-cell-type heterogeneity. *iScience* 24, 101991. [PubMed: 33490901]
30. Kim S-K, Jang SD, Kim H, Chung S, Park JK, and Kuh H-J (2020). Phenotypic Heterogeneity and Plasticity of Cancer Cell Migration in a Pancreatic Tumor Three-Dimensional Culture Model. *Cancers* 12. 10.3390/cancers12051305.
31. Ray A, Morford RK, Ghaderi N, Odde DJ, and Provenzano PP (2018). Dynamics of 3D carcinoma cell invasion into aligned collagen. *Integr. Biol* 10, 100–112.
32. Danuser G, Allard J, and Mogilner A (2013). Mathematical modeling of eukaryotic cell migration: insights beyond experiments. *Annu. Rev. Cell Dev. Biol* 29, 501–528. [PubMed: 23909278]
33. Janes KA, Gaudet S, Albeck JG, Nielsen UB, Lauffenburger DA, and Sorger PK (2006). The response of human epithelial cells to TNF involves an inducible autocrine cascade. *Cell* 124, 1225–1239. [PubMed: 16564013]
34. Muzzey D, Gómez-Uribe CA, Mettetal JT, and van Oudenaarden A (2009). A systems-level analysis of perfect adaptation in yeast osmoregulation. *Cell* 138, 160–171. [PubMed: 19596242]
35. Natarajan M, Stewart JE, Golemis EA, Pugacheva EN, Alexandropoulos K, Cox BD, Wang W, Grammer JR, and Gladson CL (2006). HEF1 is a necessary and specific downstream effector of FAK that promotes the migration of glioblastoma cells. *Oncogene* 25, 1721–1732. [PubMed: 16288224]
36. Schneider IC, and Haugh JM (2006). Mechanisms of gradient sensing and chemotaxis: conserved pathways, diverse regulation. *Cell Cycle* 5, 1130–1134. [PubMed: 16760661]
37. Sachs K, Perez O, Pe'er D, Lauffenburger DA, and Nolan GP (2005). Causal protein-signaling networks derived from multiparameter single-cell data. *Science* 308, 523–529. [PubMed: 15845847]
38. Tkachenko E, Elfenbein A, Tirziu D, and Simons M (2006). Syndecan-4 clustering induces cell migration in a PDZ-dependent manner. *Circ. Res* 98, 1398–1404. [PubMed: 16675718]
39. Wu P-H, Giri A, Sun SX, and Wirtz D (2014). Three-dimensional cell migration does not follow a random walk. *Proc. Natl. Acad. Sci. U. S. A* 111, 3949–3954. [PubMed: 24594603]
40. Maiuri P, Rupprecht J-F, Wieser S, Rupprecht V, Bénichou O, Carpi N, Coppey M, De Beco S, Gov N, Heisenberg C-P, et al. (2015). Actin flows mediate a universal coupling between cell speed and cell persistence. *Cell* 161, 374–386. [PubMed: 25799384]
41. Read MN, Bailey J, Timmis J, and Chtanova T (2016). Leukocyte Motility Models Assessed through Simulation and Multi-objective Optimization-Based Model Selection. *PLoS Comput. Biol* 12, e1005082. [PubMed: 27589606]
42. Barnhart EL, Lee K-C, Keren K, Mogilner A, and Theriot JA (2011). An adhesion-dependent switch between mechanisms that determine motile cell shape. *PLoS Biol.* 9, e1001059. [PubMed: 21559321]
43. Borm B, Requardt RP, Herzog V, and Kirfel G (2005). Membrane ruffles in cell migration: indicators of inefficient lamellipodia adhesion and compartments of actin filament reorganization. *Exp. Cell Res* 302, 83–95. [PubMed: 15541728]
44. Case LB, and Waterman CM (2015). Integration of actin dynamics and cell adhesion by a three-dimensional, mechanosensitive molecular clutch. *Nat. Cell Biol* 17, 955–963. [PubMed: 26121555]
45. DiMilla PA, Stone JA, Quinn JA, Albelda SM, and Lauffenburger DA (1993). Maximal migration of human smooth muscle cells on fibronectin and type IV collagen occurs at an intermediate attachment strength. *J. Cell Biol* 122, 729–737. [PubMed: 8335696]
46. Gupton SL, and Waterman-Storer CM (2006). Spatiotemporal feedback between actomyosin and focal-adhesion systems optimizes rapid cell migration. *Cell* 125, 1361–1374. [PubMed: 16814721]
47. Huttenlocher A, Ginsberg MH, and Horwitz AF (1996). Modulation of cell migration by integrin-mediated cytoskeletal linkages and ligand-binding affinity. *J. Cell Biol* 134, 1551–1562. [PubMed: 8830782]

48. Mitchison T, and Kirschner M (1988). Cytoskeletal dynamics and nerve growth. *Neuron* 1, 761–772. [PubMed: 3078414]
49. Palecek SP, Loftus JC, Ginsberg MH, Lauffenburger DA, and Horwitz AF (1997). Integrin-ligand binding properties govern cell migration speed through cell-substratum adhesiveness. *Nature* 385, 537–540. [PubMed: 9020360]
50. Parsons JT, Horwitz AR, and Schwartz MA (2010). Cell adhesion: integrating cytoskeletal dynamics and cellular tension. *Nat. Rev. Mol. Cell Biol* 11, 633–643. [PubMed: 20729930]
51. Vicente-Manzanares M, Choi CK, and Horwitz AR (2009). Integrins in cell migration--the actin connection. *J. Cell Sci* 122, 199–206. [PubMed: 19118212]
52. Harris TH, Banigan EJ, Christian DA, Konradt C, Tait Wojno ED, Norose K, Wilson EH, John B, Weninger W, Luster AD, et al. (2012). Generalized Lévy walks and the role of chemokines in migration of effector CD8 T cells. *Nature* 486, 545–548. 10.1038/nature11098. [PubMed: 22722867]
53. Jerison ER, and Quake SR (2020). Heterogeneous T cell motility behaviors emerge from a coupling between speed and turning in vivo. *Elife* 9. 10.7554/eLife.53933.
54. Clark RT, Nance JP, Noor S, and Wilson EH (2011). T-cell production of matrix metalloproteinases and inhibition of parasite clearance by TIMP-1 during chronic *Toxoplasma* infection in the brain. *ASN Neuro* 3, e00049. [PubMed: 21434872]
55. Shaebani MR, Reza Shaebani M, Jose R, Santen L, Stankevicius L, and Lautenschläger F (2020). Persistence-Speed Coupling Enhances the Search Efficiency of Migrating Immune Cells. *Physical Review Letters* 125. 10.1103/physrevlett.125.268102.
56. Yolland L, Burki M, Marcotti S, Luchici A, Kenny FN, Davis JR, Serna-Morales E, Müller J, Sixt M, Davidson A, et al. (2019). Persistent and polarized global actin flow is essential for directionality during cell migration. *Nat. Cell Biol* 21, 1370–1381. [PubMed: 31685997]
57. Raynaud F, Ambühl ME, Gabella C, Bornert A, Sbalzarini IF, Meister J-J, and Verkhovsky AB (2016). Minimal model for spontaneous cell polarization and edge activity in oscillating, rotating and migrating cells. *Nat. Phys* 12, 367–373.
58. Wortel IMN, Niculescu I, Koliijn PM, Gov NS, de Boer RJ, and Textor J (2021). Local actin dynamics couple speed and persistence in a cellular Potts model of cell migration. *Biophys. J* 120, 2609–2622. [PubMed: 34022237]
59. Grafinger OR, Gorshtein G, Stirling T, Geddes-McAlister J, and Coppelino MG (2021). Inhibition of β 1 integrin induces its association with MT1-MMP and decreases MT1-MMP internalization and cellular invasiveness. *Cell. Signal* 83, 109984. [PubMed: 33744418]
60. Beri P, Popravko A, Yeoman B, Kumar A, Chen K, Hodzic E, Chiang A, Banisadr A, Placone JK, Carter H, et al. (2020). Cell adhesiveness serves as a biophysical marker for metastatic potential. *Cancer Res.* 80, 901–911. [PubMed: 31857292]
61. Liu Y-J, Le Berre M, Lautenschlaeger F, Maiuri P, Callan-Jones A, Heuzé M, Takaki T, Voituriez R, and Piel M (2015). Confinement and low adhesion induce fast amoeboid migration of slow mesenchymal cells. *Cell* 160, 659–672. [PubMed: 25679760]
62. Aratyn-Schaus Y, and Gardel ML (2010). Transient frictional slip between integrin and the ECM in focal adhesions under myosin II tension. *Curr. Biol* 20, 1145–1153. [PubMed: 20541412]
63. Balaban NQ, Schwarz US, Riveline D, Goichberg P, Tzur G, Sabanay I, Mahalu D, Safran S, Bershadsky A, Addadi L, et al. (2001). Force and focal adhesion assembly: a close relationship studied using elastic micropatterned substrates. *Nat. Cell Biol* 3, 466–472. [PubMed: 11331874]
64. Doyle AD, Carvajal N, Jin A, Matsumoto K, and Yamada KM (2015). Local 3D matrix microenvironment regulates cell migration through spatiotemporal dynamics of contractility-dependent adhesions. *Nat. Commun* 6, 8720. [PubMed: 26548801]
65. Chiu C-L, Digman MA, and Gratton E (2013). Cell matrix remodeling ability shown by image spatial correlation. *J. Biophys* 2013, 532030. [PubMed: 23935614]
66. Wisdom KM, Adebowale K, Chang J, Lee JY, Nam S, Desai R, Rossen NS, Rafat M, West RB, Hodgson L, et al. (2018). Matrix mechanical plasticity regulates cancer cell migration through confining microenvironments. *Nat. Commun* 9, 4144. [PubMed: 30297715]

67. Shatkin G, Yeoman B, Birmingham K, Katira P, and Engler AJ (2020). Computational models of migration modes improve our understanding of metastasis. *APL Bioeng* 4, 041505. [PubMed: 33195959]
68. Brábek J, Mierke CT, Rösel D, Veselý P, and Fabry B (2010). The role of the tissue microenvironment in the regulation of cancer cell motility and invasion. *Cell Commun. Signal* 8, 22. [PubMed: 20822526]
69. Wolf K, Mazo I, Leung H, Engelke K, von Andrian UH, Deryugina EI, Strongin AY, Bröcker E-B, and Friedl P (2003). Compensation mechanism in tumor cell migration: mesenchymal-amoeboid transition after blocking of pericellular proteolysis. *J. Cell Biol* 160, 267–277. [PubMed: 12527751]
70. Zaman MH, Trapani LM, Sieminski AL, Mackellar D, Gong H, Kamm RD, Wells A, Lauffenburger DA, and Matsudaira P (2006). Migration of tumor cells in 3D matrices is governed by matrix stiffness along with cell-matrix adhesion and proteolysis. *Proc. Natl. Acad. Sci. U. S. A* 103, 10889–10894. [PubMed: 16832052]
71. Carragher NO, Walker SM, Scott Carragher LA, Harris F, Sawyer TK, Brunton VG, Ozanne BW, and Frame MC (2006). Calpain 2 and Src dependence distinguishes mesenchymal and amoeboid modes of tumour cell invasion: a link to integrin function. *Oncogene* 25, 5726–5740. [PubMed: 16652152]
72. Jedeszko C, Sameni M, Olive MB, Moin K, and Sloane BF (2008). Visualizing protease activity in living cells: from two dimensions to four dimensions. *Curr. Protoc. Cell Biol* Chapter 4, Unit 4.20.
73. Velez DO, Ranamukhaarachchi SK, Kumar A, Modi RN, Lim EW, Engler AJ, Metallo CM, and Fraley SI (2019). 3D collagen architecture regulates cell adhesion through degradability, thereby controlling metabolic and oxidative stress. *Integr. Biol* 11, 221–234.
74. Truong HH, Xiong J, Ghotra VPS, Nirmala E, Haazen L, Le Dévédec SE, Balcio lu HE, He S, Snaar-Jagalska BE, Vreugdenhil E, et al. (2014). β 1 integrin inhibition elicits a prometastatic switch through the TGF β -miR-200-ZEB network in E-cadherin-positive triple-negative breast cancer. *Sci. Signal* 7, ra15. [PubMed: 24518294]
75. Heinrich D, Youssef S, Schroth-Diez B, Engel U, Aydin D, Blümmel J, Spatz JP, and Gerisch G (2008). Actin-cytoskeleton dynamics in non-monotonic cell spreading. *Cell Adh. Migr* 2, 58–68. [PubMed: 19262103]
76. Mendoza MC, Er EE, Zhang W, Ballif BA, Elliott HL, Danuser G, and Blenis J (2011). ERK-MAPK drives lamellipodia protrusion by activating the WAVE2 regulatory complex. *Mol. Cell* 41, 661–671. [PubMed: 21419341]
77. Govindaraju P, Todd L, Shetye S, Monslow J, and Puré E (2019). CD44-dependent inflammation, fibrogenesis, and collagenolysis regulates extracellular matrix remodeling and tensile strength during cutaneous wound healing. *Matrix Biol.* 75–76, 314–330.
78. Osuala KO, Ji K, Mattingly RR, and Sloane BF (2019). Breast cancer: proteolysis and migration. *Adv. Exp. Med. Biol* 1152, 401–411. [PubMed: 31456196]
79. Franck C, Maskarinec SA, Tirrell DA, and Ravichandran G (2011). Three-dimensional traction force microscopy: a new tool for quantifying cell-matrix interactions. *PLoS One* 6, e17833. [PubMed: 21468318]
80. Legant WR, Choi CK, Miller JS, Shao L, Gao L, Betzig E, and Chen CS (2013). Multidimensional traction force microscopy reveals out-of-plane rotational moments about focal adhesions. *Proc. Natl. Acad. Sci. U. S. A* 110, 881–886. [PubMed: 23277584]
81. Munevar S, Wang Y, and Dembo M (2001). Traction force microscopy of migrating normal and H-ras transformed 3T3 fibroblasts. *Biophys. J* 80, 1744–1757. [PubMed: 11259288]
82. Zanotelli MR, Zhang J, Ortiz I, Wang W, Chada NC, and Reinhart-King CA (2022). Highly motile cells are metabolically responsive to collagen density. *Proc. Natl. Acad. Sci. U. S. A* 119, e2114672119. [PubMed: 35471912]

Highlights:

Data-driven modeling reveals three modes of migration speed and persistence coupling.

Migration trajectory anisotropy is a function of speed and persistence uncoupling.

Integrin beta 1 regulates migration speed and persistence coupling.

Uncoupled speed and persistence reflects uncoupled protrusions and matrix remodeling.

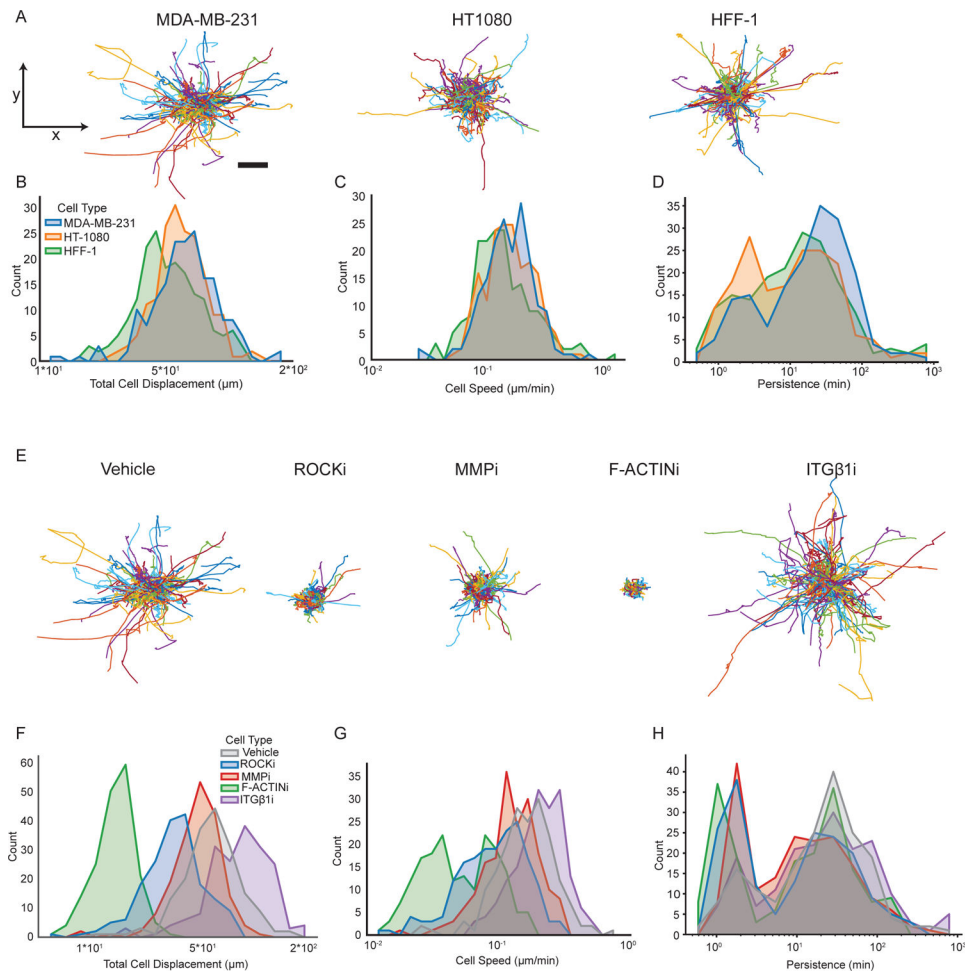


Figure 1. Cell migration is heterogeneous and less common behaviors can be enriched by perturbing biophysical processes that dictate cell-ECM interactions

(A) Cell tracking trajectories of MDA-MB-231, HT1080, and HFF-1 cells in collagen I shows heterogeneous migration behavior, highlighted by the distributions of (B) total displacement, (C) persistence, and (D) speed. Scale bar = 20 μm. N = 3 biological replicates, n = 180 cells for each cell type. (E) Trajectories of MDA-MB-231 cells from 3D cultures treated with vehicle (DMSO 0.1%), ROCK inhibitor (10 μM Y-27632), MMP inhibitor (10 μM Marimastat + GM6001), F-Actin inhibitor (5 μM Latrunculin B), or ITGB1 blocking antibody (5 μg ml⁻¹ P5D2). N = 3 biological replicates, n = 180 cells for each treatment condition. Distributions of the resulting (F) total cell displacement, (G) persistence time, and (H) cell speed show how each treatment population shifts while still retaining heterogeneity and overlap between populations. See also Figure S1

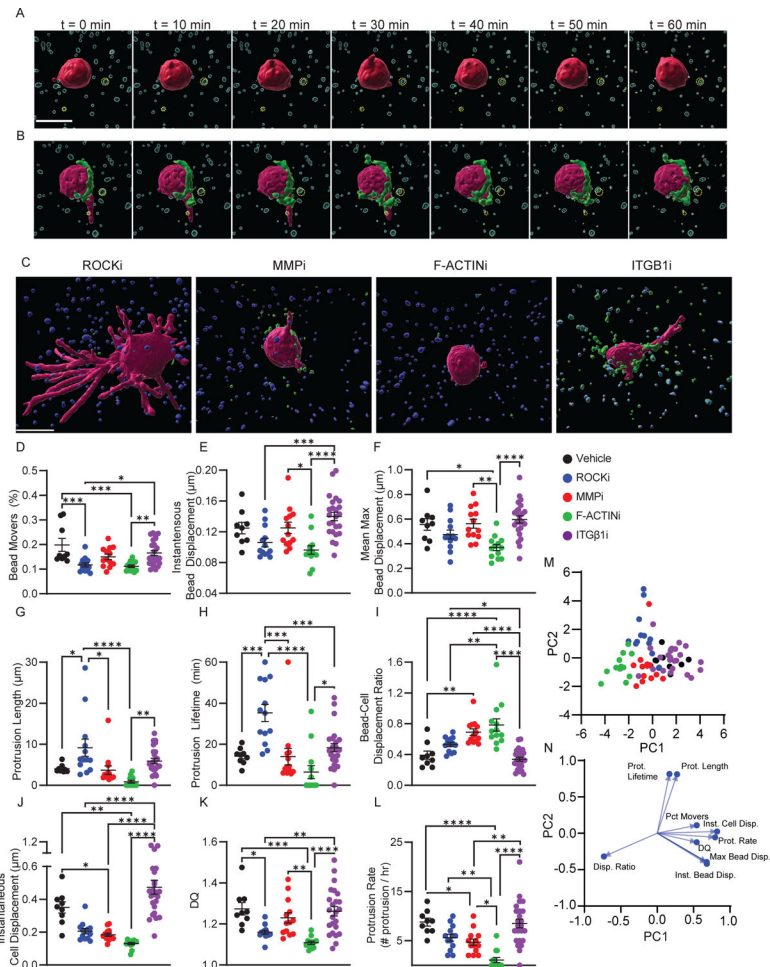


Figure 2. Cells-ECM interaction measurements capture whole-cell biophysical behavior
(A-B) Time-series snapshots showing 3D reconstructions of micrographs of individual cells (red), beads (blue), and dye-quenched (DQ) collagen (green) at 10-minute intervals highlight biophysical differences among individual MDA-MB-231 cells embedded in 2.5 mg ml⁻¹ collagen I matrices. The cell in (A) remains mostly rounded with little bead movement, while the cell in (B) retracts a protrusion, pulls beads, and has more DQ signal. Dotted yellow circles outline the original positions of example beads. Scale bar = 20 μ m. **(C)** 3D reconstructions of representative cells from each inhibitor-treated population highlight changes to cell shape and matrix remodeling. **(D-L)** Comparison of the inhibitor-treated groups for each cell-ECM measurement. n = 9 for each treatment group. Statistical significance was determined using one-way ANOVA with Tukey Post-Test. * p<0.05; ** p<0.01; *** p<0.001. **(M)** Top two principal component scores for each cell show the clustering of cells based on inhibitor treatments. **(N)** The loadings along the first two principal components shows the relative contributions of each cell-ECM interaction in the PCA. See also Figure S2 and S3.

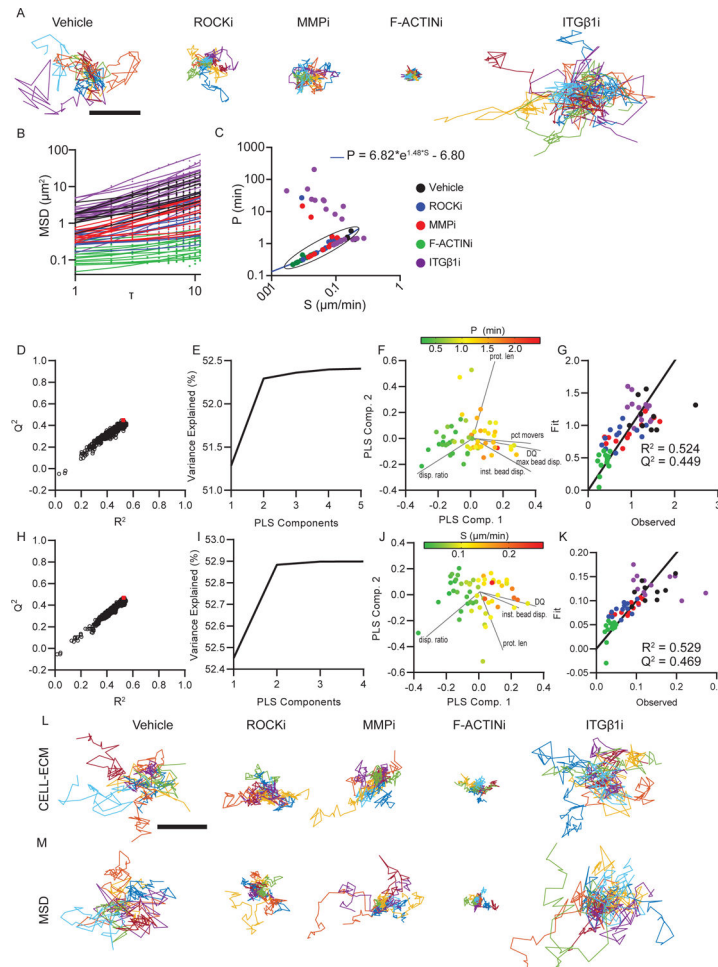


Figure 3. Cell trajectories are well-modeled by the PRW when S and P are coupled
(A) Trajectories of individual MDA cells treated with vehicle, F-ACTINi, ROCKi, MMPi, or ITGB1i show heterogeneity in migration paths. Scale bar = 5 μ m. **(B)** MSDs of individual cells fit using the persistent random walk (PRW) model. **(C)** Graph of PRW parameters cell speed (S) versus persistence time (P). Line indicates regression of points in the circled region to the “universal coupling between speed and persistence” (UCSP) equation. S and P are coupled for the majority of the cells, though a large population does not follow this trend. PLSR was performed using every possible combination of measurements to fit cell-ECM interactions to persistence. **(D)** The fit (R^2) vs. predictive ability (Q^2) of all possible regressions for persistence (P), and the optimal predictive model is shown by the red square. **(E)** The best predictive model for P accounts for more than 52% of the variance using just the first two PLS components. **(F)** Plotting the PLS score of each cell along these two components shows separation of persistence and the cell-ECM interaction measurement component loading projections. Loadings for the two beads displacement measurements overlap. **(G)** Observed vs. fitted values of z-normalized persistence show overall good agreement. **(H-L)** The same PLSR approach was applied for cell speed. **(H)** The fit (R^2) vs. predictive ability (Q^2) of all possible regressions of cell speed (S), and the optimal predictive model is shown by the red square. **(I)** This model can account for more than 52% of the total

variance in cell speed using just the first two PLS components. **(J)** Plotting the PLS score of each cell along these two components shows separation of cell speed and the cell-ECM interaction measurement component loading projections. **(K)** Observed vs. fitted values of z-normalized cell speed show overall good agreement. **(L)** Trajectories simulated using the PRW from S and P values extracted from the MSD fit (top row) or predicted by the PLSR model using cell-ECM interactions (bottom row) recreate the heterogeneity and migration trends observed experimentally. Scale bar = 5 μ m. See also Figure S4 and S5.

Author Manuscript

Author Manuscript

Author Manuscript

Author Manuscript

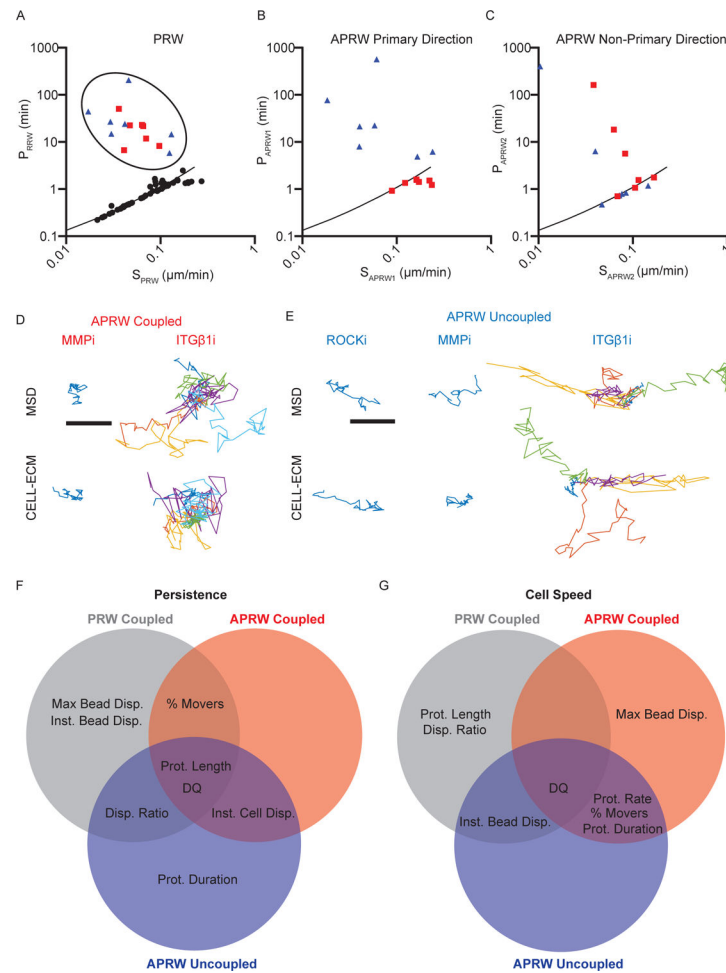


Figure 4. Trajectories of cells whose speed and persistence are not well coupled are predicted by a distinct set of cell-ECM interactions

(A) Graph of persistence time versus speed, with the cells that do not follow the UCSP in the PRW model circled. (B-C) Modeling these cells with the anisotropic persistent random walk model (APRW) identifies coupling between speed and persistence in the primary direction of migration (B), as well as the non-primary direction (C). Cells that are well coupled in the primary direction are shown as red squares, while those that are not are represented by the blue triangles. (D-E) PLSR modeling achieves a strong fit and high predictive accuracy when these two populations are separated. Simulated trajectories using PLSR models for cells coupled in the primary direction (D) or uncoupled (E) recreate migration behaviors. Scale bar = $5\mu\text{m}$. Venn Diagram of which cell-ECM measurements were used in the PLSR model to predict (F) persistence or (G) speed as determined by the PRW model and the persistence in the primary direction of migration for the cells modeled using APRW. See also Figure S6, S7, and Table S1.

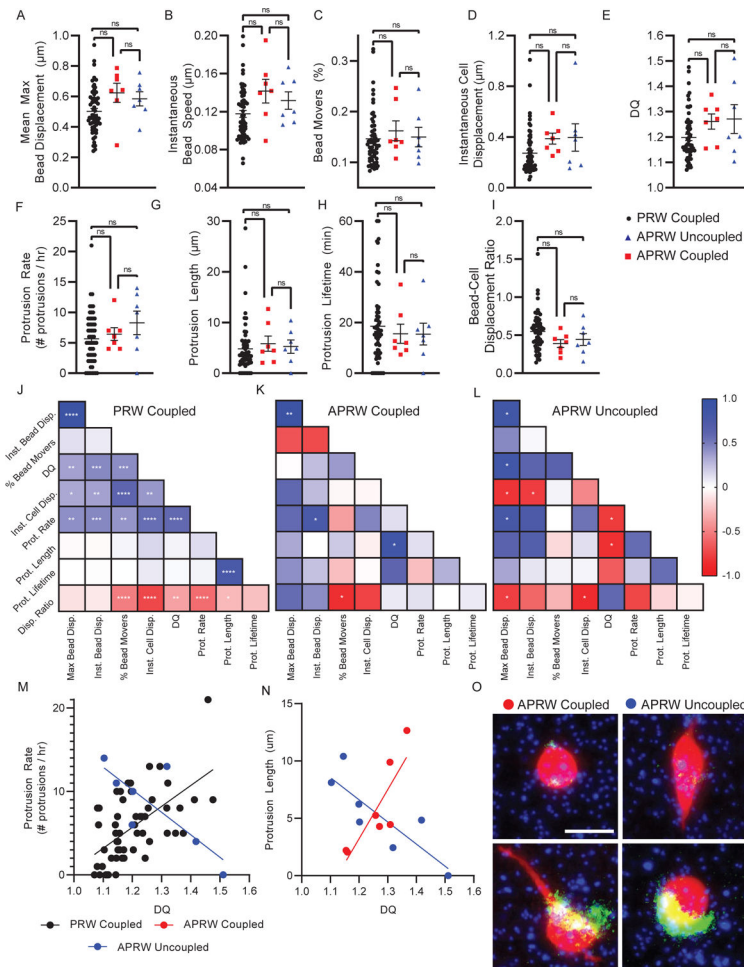


Figure 5. Matrix remodeling coordination with adhesion and cell protrusion underly the differing modes of cell migration

(A-I) Cell-ECM measurements of individual cells grouped by their speed vs. persistence coupling behavior. The two APRW groups match the expected shifts from cell populations comprised predominantly of ITGB1i cells. No significant differences between the APRW groups were observed. (J-L) Heatmap of Pearson correlations between cell-ECM measurements of cells displaying PRW S vs. P coupling (J), APRW coupling in the primary direction (K), and APRW uncoupled (L). Color indicates the Pearson ρ -value, the strength of the correlation, and p-value is indicated by * $p < 0.05$; ** $p < 0.01$; *** $p < 0.001$; **** $p < 0.0001$. (M) Correlation between DQ and protrusion rate measurements for cells in the PRW coupled and APRW uncoupled regimes. (N) Correlation between DQ and protrusion length for cells in the APRW coupled or uncoupled regimes. (O) Representative images of cells in the APRW coupled or uncoupled regimes demonstrating the opposite relationships between matrix remodeling and protrusion of the two groups. Scale bar = 20 μm.

KEY RESOURCES TABLE

REAGENT or RESOURCE	SOURCE	IDENTIFIER
Antibodies		
Rabbit monoclonal [EPR638Y] to ROCK1	Abcam	Cat#ab134181; RRID:AB_2920582
Rabbit monoclonal to GAPDH	Cell Signaling Technologies	Cat#2118; RRID:AB_561053
Mouse monoclonal [12G10] to Integrin beta 1	Abcam	Cat#ab30394; RRID:AB_775726
Mouse monoclonal [P5D2] to Integrin beta 1	Millipore	Cat#MAB1959; RRID:AB_94462
Bacterial and Virus Strains		
DH5a chemically competent cells	Thermo Fisher	Cat#18258012
Chemicals, Peptides, and Recombinant Proteins		
Y27632	Millipore	Cat#509228
DMSO	Sigma-Aldrich	Cat#D2650
Marimastat	Abcam	Cat#ab141276
GM6001	Millipore	Cat#CC1000
Latrunculin B	Tocris	Cat#3974
Collagen I	Corning	Cat#CB354249
DQ Collagen I	Invitrogen	Cat#D12060
Critical Commercial Assays		
Lipofectamine 3000	Thermo Fisher	Cat#L3000008
Deposited Data		
Original western blot images	This paper	Mendeley: https://doi.org/10.17632/r2sm43trbr.1
Experimental Models: Cell Lines		
MDA-MB-231	ATCC	Cat#HTB-26
HT1080	ATCC	Cat#CCL-121
HFF-1	ATCC	Cat#SCRC-1041
Recombinant DNA		
pLV mCherry	Addgene	RRID:Addgene_36084
psPAX2	Addgene	RRID:Addgene_12260
pMD2.G	Addgene	RRID:Addgene_12259
pRS shROCK1	Origene	Cat#TG309775
Software and Algorithms		
Fiji/ImageJ 2	NIH	RRID:SCR_002285
MATLAB R2022a	Mathworks, Inc.	RRID:SCR_001622
Metamorph	Molecular Devices	RRID:SCR_002368
NIS-Elements	Nikon	RRID:SCR_014329
Prism 9	Graphpad	RRID:SCR_002798
Imaris	Oxford Instruments	RRID:SCR_007370
Partial least squares regression analysis	This paper	Mendeley: https://doi.org/10.17632/r2sm43trbr.1
Cell trajectory and random walk analysis	Wu et al. ³⁹	https://doi.org/10.1073/pnas.1318967111

REAGENT or RESOURCE	SOURCE	IDENTIFIER
Other		
Blue fluorescent 1µm polystyrene microsphere	Invitrogen	Cat# F13080

Author Manuscript

Author Manuscript

Author Manuscript

Author Manuscript

Table 1:

Biophysical measurements used to quantify overall cell-ECM interaction state of a cell

Measurements	Method	Biophysical Process Readout
% bead movers, maximum bead displacement, instantaneous bead displacement	Fluorescent matrix-embedded beads (blue)	Cellular contractility against the matrix
DQ	Dye-Quenched (DQ) collagen I fluorescence (green)	Remodeling of matrix by cells
Instantaneous cell displacement, protrusion rate, protrusion lifetime, and maximum protrusion length	Cells transduced with mCherry fluorescent protein (red)	Cytoskeletal activity
Bead-cell displacement ratio	Ratio of instantaneous bead displacement over instantaneous cell displacement	Coupling between cell and the surrounding ECM

Author Manuscript

Author Manuscript

Author Manuscript

Author Manuscript

Table 2:

Principal component analysis loadings of cell-ECM interactions

	Loadings									
	Eigen value	Mean Max Bead Displacement	Inst. Bead Displacement	Pct Bead Movers	Inst. Cell Displacement	DQ	Protrusion Rate	Protrusion Length	Protrusion Duration	Bead-cell displacement ratio
PC1	2.835	-0.932	-0.942	0.155	-0.226	-0.782	0.064	-0.244	-0.228	-0.527
PC2	2.242	0.203	0.169	0.126	0.678	0.218	-0.203	-0.804	-0.823	-0.533
PC3	1.498	-0.047	-0.009	0.112	-0.606	0.031	-0.773	-0.351	-0.308	0.547
PC4	1.119	0.074	-0.163	0.938	-0.019	0.312	-0.109	0.114	0.227	-0.181
PC5	0.607	-0.053	-0.025	-0.168	0.262	-0.049	-0.586	0.275	0.182	-0.228
PC6	0.379	0.191	0.130	0.180	0.147	-0.484	-0.030	-0.089	0.103	0.132
PC7	0.169	0.010	0.001	-0.071	-0.057	0.047	-0.015	-0.269	0.280	-0.086
PC8	0.086	-0.168	0.002	0.026	0.158	0.051	0.006	-0.043	0.044	0.159
PC9	0.066	-0.125	0.200	0.037	-0.058	-0.022	0.001	0.013	-0.005	-0.071